

# Study of Excited $\Xi^-$ Baryons in $\bar{p}p$ -Collisions with $\overline{\text{PANDA}}$

Authors:

Jennifer Pütz, Albrecht Gillitzer, James Ritman, Tobias  
Stockmanns

---

# Contents

<b>1</b>	<b>Introduction</b>	<b>1</b>
<b>2</b>	<b>Event generation</b>	<b>2</b>
<b>3</b>	<b>Analysis</b>	<b>6</b>
3.1	Final state particles . . . . .	6
3.2	Reconstruction of $\Lambda$ and $\bar{\Lambda}$ . . . . .	8
3.3	Reconstruction of $\Xi^-$ and $\bar{\Xi}^+$ . . . . .	12
3.4	Reconstruction of $\Xi(1820)^-$ and $\bar{\Xi}^+(1820)$ . . . . .	19
3.5	Reconstruction of the whole reaction chain . . . . .	24
<b>4</b>	<b>Background</b>	<b>27</b>
<b>5</b>	<b>Summary and Conclusion</b>	<b>29</b>
	<b>References</b>	<b>30</b>

---

# 1 Introduction

Understanding the excitation pattern of baryons is indispensable for a deep insight into the mechanism of non-perturbative QCD. Up to now only the nucleon excitation spectrum has been subject to systematic experimental studies while very little is known on excited states of double or triple strange baryons.

In studies of antiproton-proton collisions the  $\bar{\text{P}}\text{ANDA}$  experiment is well-suited for a comprehensive baryon spectroscopy program in the multi-strange and charm sector. A large fraction of the inelastic  $\bar{p}p$  cross section is associated to final states with a baryon-antibaryon pair together with additional mesons, giving access to excited states both in the baryon and the antibaryon sector.

In the present study we focus on excited  $\Xi^-$  states. For final states containing a  $\Xi^- \bar{\Xi}^+$  pair cross sections up to the order of  $\mu\text{b}$  are expected, corresponding to production rates of  $\sim 10^6/\text{d}$  at a Luminosity  $L = 10^{31} \text{ cm}^{-2} \text{ s}^{-1}$  (5% of the full value). A strategy to study the excitation spectrum of  $\Xi^-$  baryons in antiproton-proton collisions will be discussed. The reconstruction of reactions of the type  $\bar{p}p \rightarrow \Xi^{*-} \bar{\Xi}^+$  (and their charge conjugate) with the  $\bar{\text{P}}\text{ANDA}$  detector will be presented based on a selected exemplary reaction and decay channel.

---

## 2 Event generation

To study excited  $\Xi^-$  baryons the simulation of a sufficient number of signal events is needed. For this study 1.5 million signal events were generated with the event generator EvtGen. The reaction and decay tree selected for the simulation is shown in figure 2.1. If not otherwise specified, the charged conjugate process is implicitly included in the following.

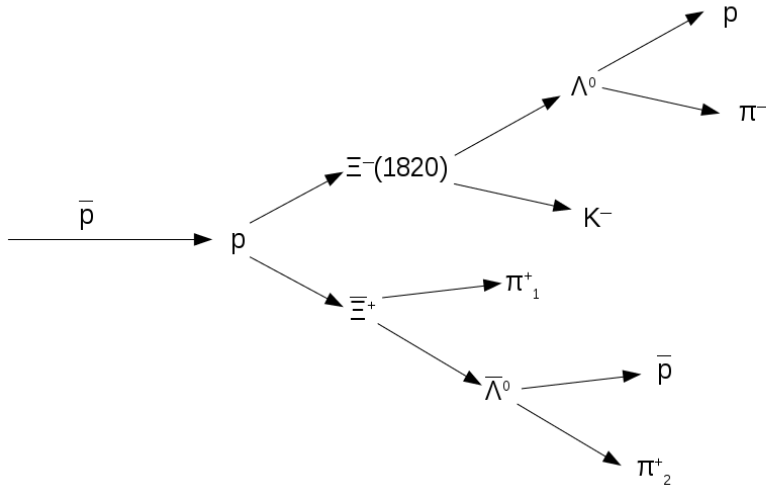


**Figure 2.1:** Reaction and decay tree selected for the simulation.

For the charge conjugate channel another 1.5 million events were generated. Table 2.1 shows the parameters used for the event generation. For the production reaction  $\bar{p}p \rightarrow \Xi(1820)^- \Xi^+$  the PHSP model, generating an isotropic angular distribution, was used, because a more realistic treatment has not yet been implemented in EvtGen. This simplification does not affect the strategy used for this study. The chosen beam momentum  $p_{\bar{p}} = 4.6 \text{ GeV}/c$  corresponds to a center-of-mass energy of

**Table 2.1:** Parameter for event generation

Parameter	Value
Beam momentum	4.6 GeV/c <sup>2</sup>
Production	PHSP
Tracking	Ideal
Particle ID	Ideal

**Table 2.2:** Used software version

Software	Version
FairSoft	mar15
FairRoot	v-15.03a
PandaRoot	trunk revision 28555
Geant	3
Genfit	1

100 MeV above the production threshold of  $\Xi(1820)^-$  and  $\bar{\Xi}^+$ . The production cross section is expected to be of the same order ( $\sim \mu\text{b}$ ) as for ground state  $\Xi^-$  production in  $\bar{p}p \rightarrow \Xi^- \bar{\Xi}^+$  [1]. This expectation is based on ground state and excited state single strange hyperons production data in  $\bar{p}p$  collisions [2].

The used software version for PandaRoot and the external software package is listed in table 2.2.

The missing  $\Xi(1820)^-$  was defined in the evt.pdl file listing the properties of particles used in EvtGen. The properties of  $\Xi(1820)^-$  are listed in table 2.3.

The distribution of the generated transverse momentum versus the longitudinal momentum for  $\Lambda$  and  $\bar{\Lambda}$  is presented in figure 2.2 and for  $\bar{\Xi}^+$  and  $\Xi(1820)^-$  in figure 2.3.

Figure 2.4 shows the Dalitz plot for the  $\Lambda$ ,  $K^-$  and  $\bar{\Xi}^+$  final states for the channel  $\bar{p}p \rightarrow \Xi(1820)^- \bar{\Xi}^+$ .

**Table 2.3:** Properties of  $\Xi(1820)^-$  and  $\bar{\Xi}^+(1820)$ . The values are taken from [3]

Particle	J	I	P	Charge	Mass	Width
$\Xi(1820)^-$	$\frac{3}{2}$	$\frac{1}{2}$	(-1)	(-1)	$(1.823 \pm 5) \text{ GeV}/c^2$	$(0.024 \pm 6) \text{ GeV}/c^2$
$\bar{\Xi}^+(1820)$	$\frac{3}{2}$	$\frac{1}{2}$	(-1)	1	$(1.823 \pm 5) \text{ GeV}/c^2$	$(0.024 \pm 6) \text{ GeV}/c^2$

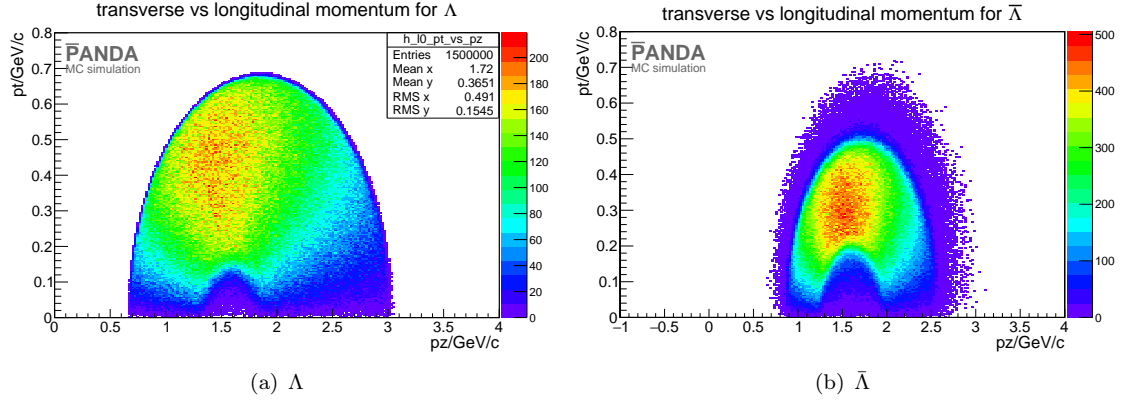


**Figure 2.2:** "PROPOSED FOR RELEASE" Figure a) shows the transverse momentum on the y axis versus the longitudinal momentum on the x axis for  $\Lambda$ . Figure b) shows the same distribution for  $\bar{\Lambda}$ .

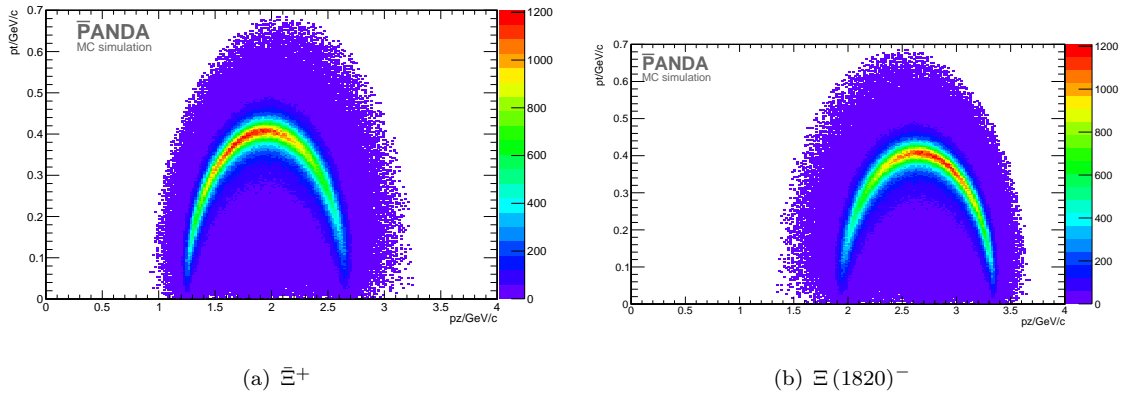


**Figure 2.3:** "PROPOSED FOR RELEASE" Figure a) shows transverse versus the longitudinal momentum distribution for  $\Xi^+$ . Figure b): transverse versus longitudinal momentum distribution for  $\Xi(1820)^-$ .

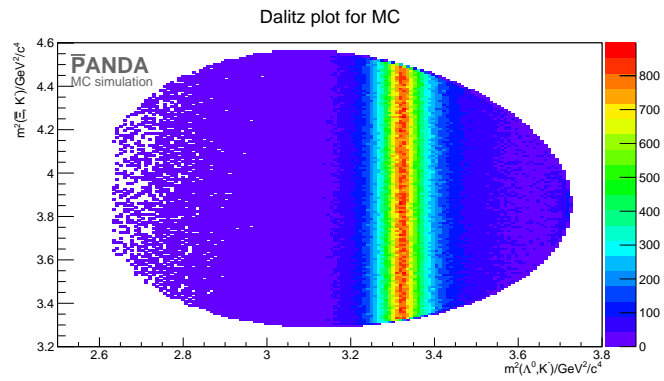


**Figure 2.4:** "PROPOSED FOR RELEASE"  $\Xi^- \Lambda K^-$  Dalitz plot for generated events. On the x axis is the squared mass of  $\Lambda K^-$  system and on the y axis there is the squared mass of  $\Xi^- K^-$  system.

---

## 3 Analysis

To reconstruct all the particles involved in the reaction we start with the final state particles and go backwards through the reaction chain.

### 3.1 Final state particles

The selected final state particle are protons, anti-protons,  $\pi^-$ ,  $\pi^+$ ,  $K^-$  and  $K^+$  mesons. For the reconstruction of these particles an ideal tracking was used. Ideal tracking means that the hit points caused by a particle track are grouped based on the generated particle information. To achieve a more realistic reconstruction efficiency only particles with at least 4 hits in any inner tracking detector (MVD, STT and GEM) are selected. The selection criterion is chosen because three hits are needed to defining a circle. A fourth hit point is then a validation of the track hypothesis. The particle identification (PID) is also ideal meaning that the true particle gets the probability  $P = 1$ , the others  $P = 0$ . The selection criterion is set to 'best'.

The reconstruction efficiency and the momentum resolution for the final state particle is shown in table 3.1 and figure 3.1. All reconstruction efficiencies are calculated with the MC matched particles.

Table 3.2 shows the reconstruction efficiency and the momentum resolution for the charge conjugate channel.

**Table 3.1: "PROPOSED FOR RELEASE"** Reconstruction efficiency and momentum resolution for  $\bar{p}p \rightarrow \Xi(1820)^- \bar{\Xi}^+$

final state	N/%	$\sigma_N^{\text{stat.}}/\%$	$\frac{\sigma_p}{p}/\%$	$\sigma_{\frac{\sigma_p}{p}}/\%$
$\pi^-$	83.48	$10^{-8}$	1.53	$3 \cdot 10^{-3}$
$\pi_1^+$ ( $\bar{\Xi}^+$ )	80.93	$10^{-8}$	1.38	$3 \cdot 10^{-3}$
$\pi_2^+$ ( $\bar{\Lambda}$ )	83.07	$10^{-8}$	1.49	$3 \cdot 10^{-3}$
$K^-$	78.59	$10^{-8}$	1.58	$3 \cdot 10^{-3}$
p	84.39	$10^{-8}$	1.61	$4 \cdot 10^{-3}$
$\bar{p}$	78.25	$10^{-8}$	1.45	$4 \cdot 10^{-3}$



**Table 3.2: "PROPOSED FOR RELEASE"** Reconstruction efficiency and momentum resolution for  $\bar{p}p \rightarrow \bar{\Xi}^+(1820) \Xi^-$

final state	N/%	$\sigma_N^{\text{stat.}}/\%$	$\frac{\sigma p}{p}/\%$	$\sigma_{\frac{\sigma p}{p}}/\%$
$\pi^+$	82.96	$10^{-8}$	1.54	$2 \cdot 10^{-3}$
$\pi_1^- (\Xi^-)$	80.40	$10^{-8}$	1.38	$2 \cdot 10^{-3}$
$\pi_2^- (\Lambda)$	82.69	$10^{-8}$	1.49	$3 \cdot 10^{-3}$
$K^+$	83.27	$10^{-8}$	1.58	$3 \cdot 10^{-3}$
p	80.71	$10^{-8}$	1.55	$4 \cdot 10^{-3}$
$\bar{p}$	80.93	$10^{-8}$	1.60	$4 \cdot 10^{-3}$

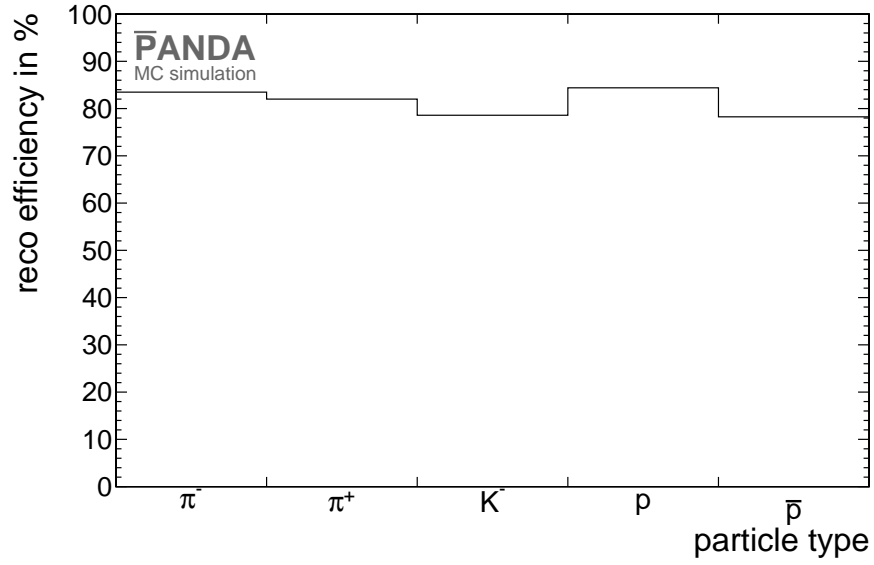


**Figure 3.1: "PROPOSED FOR RELEASE"** Reconstruction efficiency for final state particles. The x axis shows the particle type. On the y axis the fraction of reconstructed particles is shown.

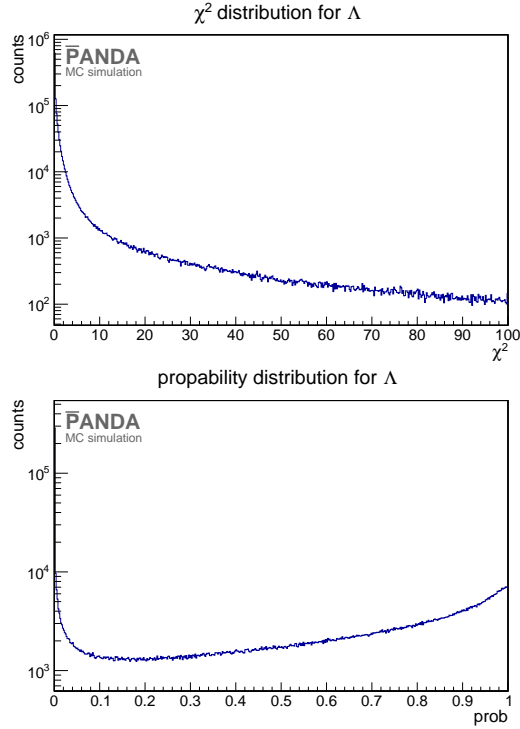


**Figure 3.2:** **"PROPOSED FOR RELEASE"** The upper plot shows the  $\chi^2$  distribution and the lower plot shows the probability distribution for the  $\Lambda$  vertex fit.

## 3.2 Reconstruction of $\Lambda$ and $\bar{\Lambda}$

### Selection

For the reconstruction of  $\Lambda$  hyperons a proton and a  $\pi^-$  meson are combined and for the reconstruction of  $\bar{\Lambda}$  a  $\bar{p}$  and a  $\pi^+$  are combined. After combining the daughter particles a mass cut is performed. Only those candidates are chosen which have a mass within a window of  $0.3 \text{ GeV}/c^2$  symmetric to the nominal  $\Lambda$  mass, i.e., a mass within  $m = 1.116 \pm 0.15 \text{ GeV}/c^2$ .

A vertex constraint fit with the PndKinVtxFitter is performed on the selected candidate. This means that the tracks of the daughter particles are fitted to a common vertex point. The  $\chi^2$  and probability distribution of the vertex fit for  $\Lambda$  candidates is shown in figure 3.2.

In the probability distribution one can see an increasing number of events for probabilities approaching a value of one. This feature is not the vertex fit itself, as was shown by tests based on the so-called "poormantrack" algorithm [4].

A mass constraint fit is performed on the fitted candidate. For this mass constraint fit the

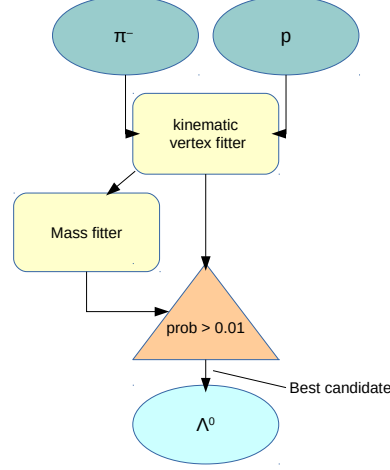


**Figure 3.3: "PROPOSED FOR RELEASE"** Scheme for  $\Lambda$  reconstruction

kinematic fitter PndKinFitter is used. After using both fitters the selection criterion is set. Only those particles which have a probability larger than 1% in both fitters are selected. A scheme which shows how the events are selected can be found in figure 3.3. If there is more than one candidate left after these cuts, the candidate with the lowest  $\chi^2$  is chosen.

## Results

In this paragraph the  $\Lambda$  and  $\bar{\Lambda}$  sample obtained with the chosen selection criteria is presented. The mass distributions corresponding to the different cuts are shown in figure 3.4 and figure 3.5 for  $\Lambda$  and  $\bar{\Lambda}$ , respectively.

The reconstructed mass can be determined by performing a double Gaussian fit on the mass distribution obtained after all cuts. The mass distribution and the double Gaussian fit are shown for  $\Lambda$  candidates in figure 3.6.

The peak position of the Gaussian fit is taken as the value of the reconstructed mass. The reconstructed masses are  $m_{\Lambda} = (1.1158 \pm 0.0021) \text{ GeV}/c^2$  and  $m_{\bar{\Lambda}} = (1.1158 \pm 0.0021) \text{ GeV}/c^2$  for  $\Lambda$  and  $\bar{\Lambda}$ , respectively. Figure 3.7 shows the transverse momentum versus the longitudinal momentum.

After all cuts the reconstruction efficiency is 40.48% for  $\Lambda$  and 33.42% for  $\bar{\Lambda}$ . The difference

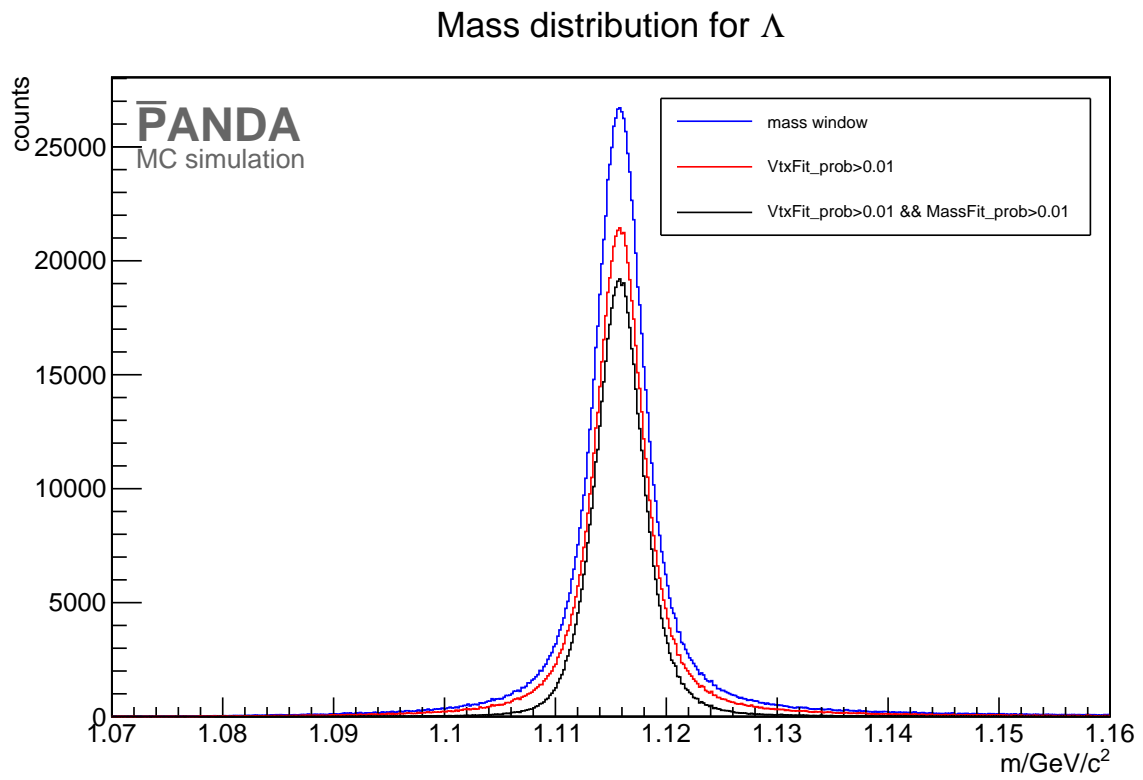


**Figure 3.4:** "PROPOSED FOR RELEASE" Mass distribution of  $\Lambda$  after the mass cut (blue), after the vertex fit cut (red) and after all cuts (black).

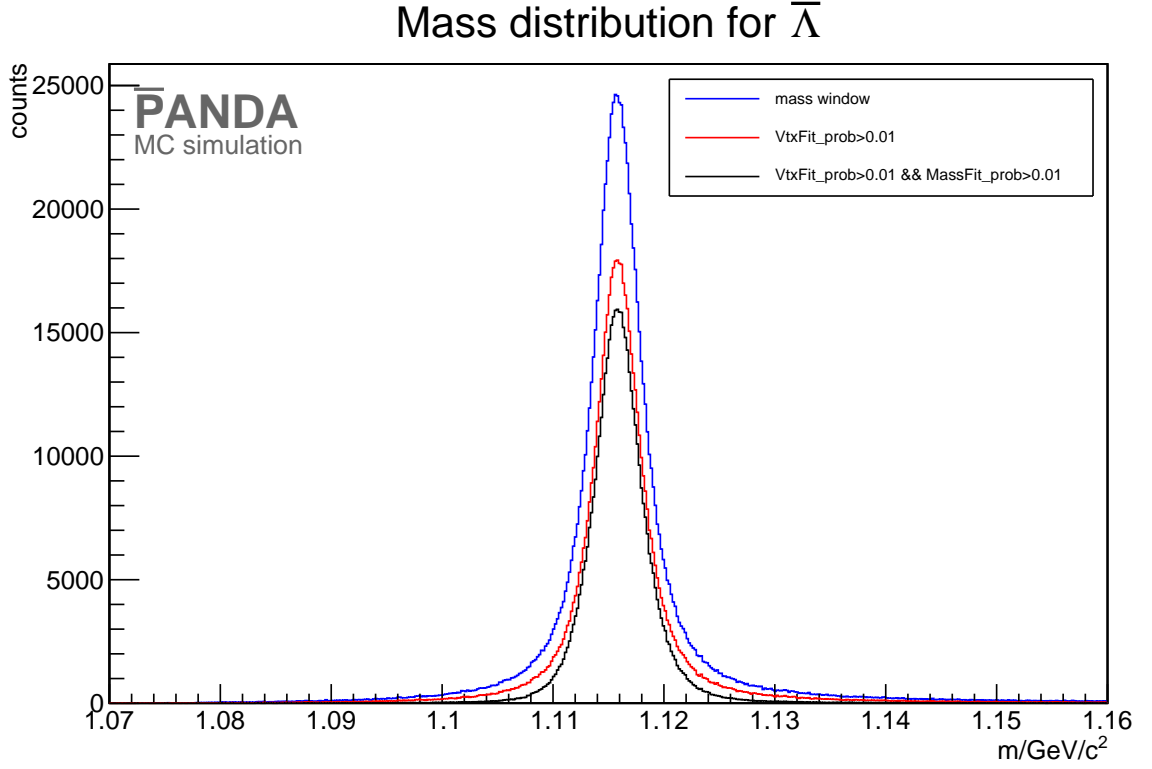


**Figure 3.5:** "PROPOSED FOR RELEASE" Mass distribution of  $\bar{\Lambda}$  after the mass cut (blue), after the vertex fit cut (red) and after all cuts (black).

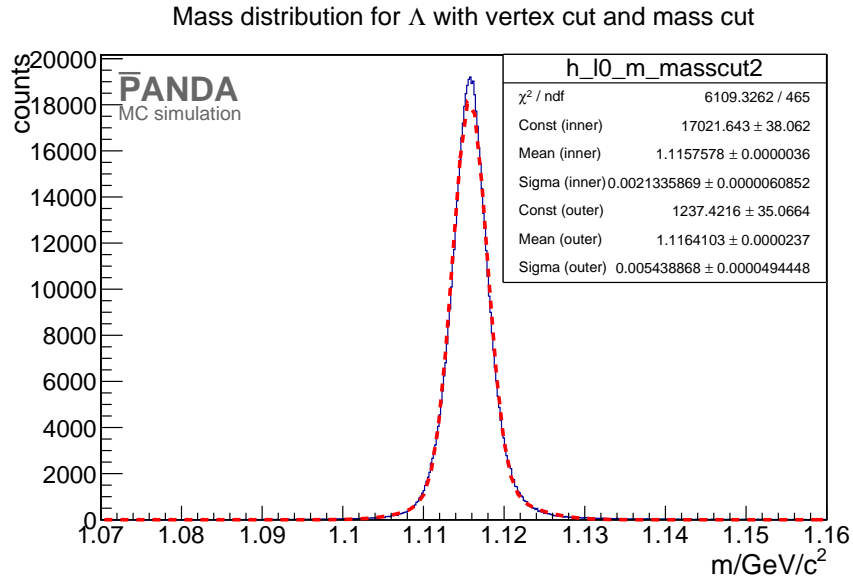


**Figure 3.6:** "PROPOSED FOR RELEASE" Mass distribution (blue histogram) for  $\Lambda$  fitted with a double Gaussian fit (red dashed line).

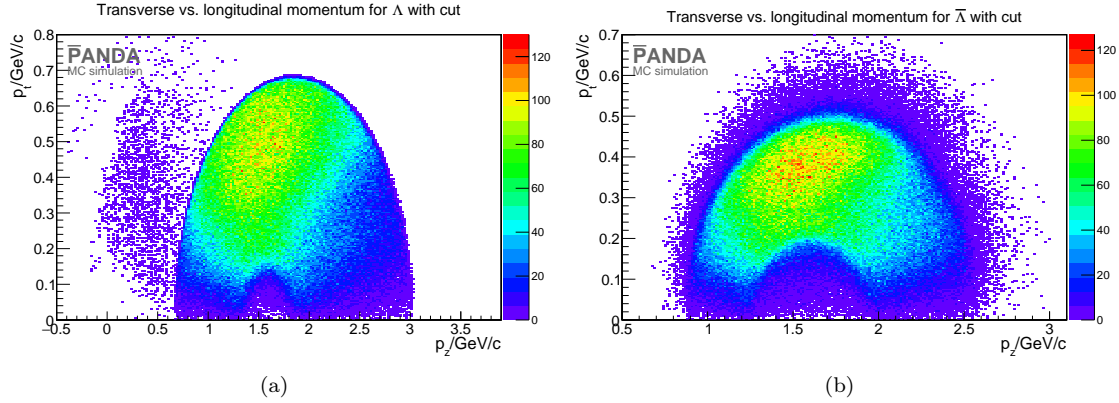


**Figure 3.7: "PROPOSED FOR RELEASE"** Figure a): transverse versus longitudinal momentum for  $\Lambda$ . Figure b): transverse versus longitudinal momentum for  $\bar{\Lambda}$ .

in the reconstruction efficiencies for  $\Lambda$  and  $\bar{\Lambda}$  is caused by the different decay lengths of their mother particles.  $\Lambda$  is emitted by the  $\Xi(1820)^-$  which has a very short decay length while the decay length of  $\Xi^+$  is  $c\tau = 4.91$  cm [3]. The decay length of  $\Lambda$  and  $\bar{\Lambda}$  is  $c\tau = 7.98$  cm, so that the final state particles of  $\bar{\Lambda}$  are produced more downstream than the final state particles of  $\Lambda$ . This can be also seen in figure 3.8. The final state particles of  $\bar{\Lambda}$  are produced at the edge of the MVD detector so that the reconstruction efficiency for these particles is reduced. An extension of the MVD with two more discs the so-called "Lambda-Discs" might improve the reconstruction efficiencies for  $\Lambda$  and  $\bar{\Lambda}$ .

### 3.3 Reconstruction of $\Xi^-$ and $\bar{\Xi}^+$

#### Selection

The reconstruction of  $\Xi^-$  and  $\bar{\Xi}^+$  follows a scheme similar to the reconstruction of  $\Lambda$  and  $\bar{\Lambda}$ . For  $\bar{\Xi}^+$   $\bar{\Lambda}$  and  $\pi^+$  are recombined, for  $\Xi^-$  in the charge conjugate channel  $\Lambda$  and  $\pi^-$ . In case of the correct selection both the  $\pi^-$  or  $\pi^+$  candidate as daughter particle of  $\Lambda$  or  $\bar{\Lambda}$ , respectively, only one  $\pi^-$  or  $\pi^+$  candidate remains within the primary particles of the reaction chain, which must be the daughter particle of  $\Xi^-$  or  $\bar{\Xi}^+$ , respectively. The correct selection of the  $\Lambda$  and  $\bar{\Lambda}$  daughter pions is assured by the choice of the best fitted  $\Lambda$  and  $\bar{\Lambda}$  candidates, as described in section 3.2. The pions associated to the  $\Lambda$  and  $\bar{\Lambda}$  decay are removed from the pion candidate lists used for the reconstruction of  $\Xi^-$  and  $\bar{\Xi}^+$ . After combining the daughter particles a mass cut is performed corresponding to a window with a width of  $0.3 \text{ GeV}/c^2$  symmetric around the  $\Xi^-$  mass  $m_{\Xi} = 1.32171 \text{ GeV}/c^2$  [3]. The fitting scheme is the same as for  $\Lambda$  and  $\bar{\Lambda}$  and is shown in figure 3.9. After the mass cut the daughter particles are fitted to a common vertex with the PndKinVtxFitter. The

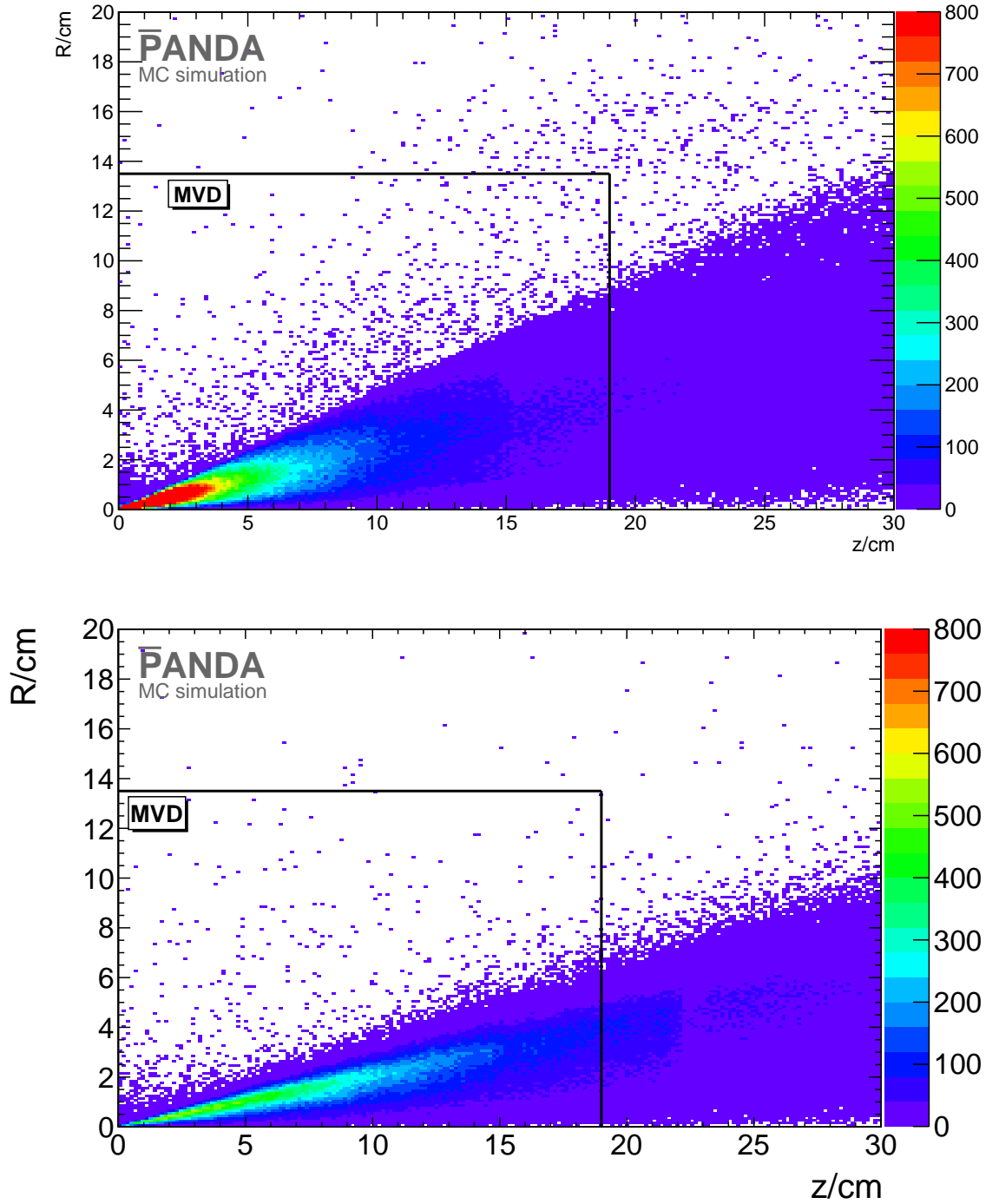


**Figure 3.8:** **"PROPOSED FOR RELEASE"** Decay vertex position of  $\Lambda$  (upper plot) and  $\bar{\Lambda}$  (lower plot). In both plots the x axis shows the  $z$  coordinate (along the beam axis) of the decay vertex while the y axis shows its radial coordinate (the origin of the coordinate system  $s$  defined by the primary vertex). The black horizontal and vertical lines mark the radial and longitudinal extension of the MVD.

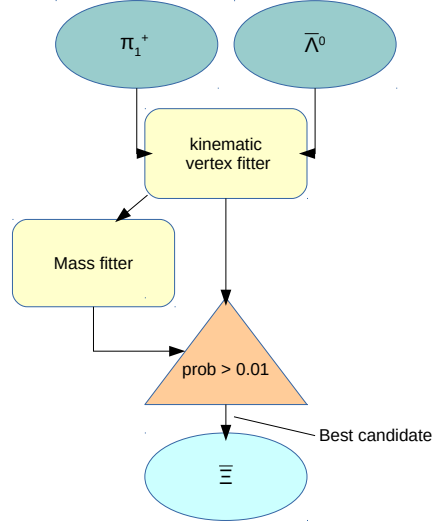


**Figure 3.9:** "PROPOSED FOR RELEASE" Scheme for  $\Xi^+$  reconstruction

resulting candidates are used to perform the mass constraint fit.  
 Only those particles are selected which have a probability of more than 1 % in both fitters.  
 Figure 3.10 shows exemplarily the cut on the vertex fit probability for  $\Xi^+$ .  
 If there is more than one candidate left after all cuts, e.g. due to additional pions produced  
 in secondary interactions, the candidate with the lowest  $\chi^2$  is chosen.

## Results

The vertex resolution after all cuts is shown in table 3.3.  
 It is determined by calculating the full width at half maximum (FWHM) of the distribution.

**Table 3.3:** "PROPOSED FOR RELEASE" Vertex resolution for  $\Xi^+$  and  $\Xi^-$  (charge conjugate. channel)

position	$\Xi^+$	$\Xi^-$ (from charge conjugate.)
x/cm	0.052	0.056
y/cm	0.052	0.052
z/cm	0.19	0.2



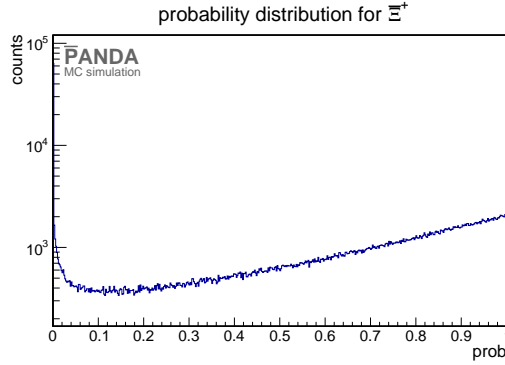


**Figure 3.10:** "PROPOSED FOR RELEASE" probability distribution for  $\bar{\Xi}^+$  reconstruction.

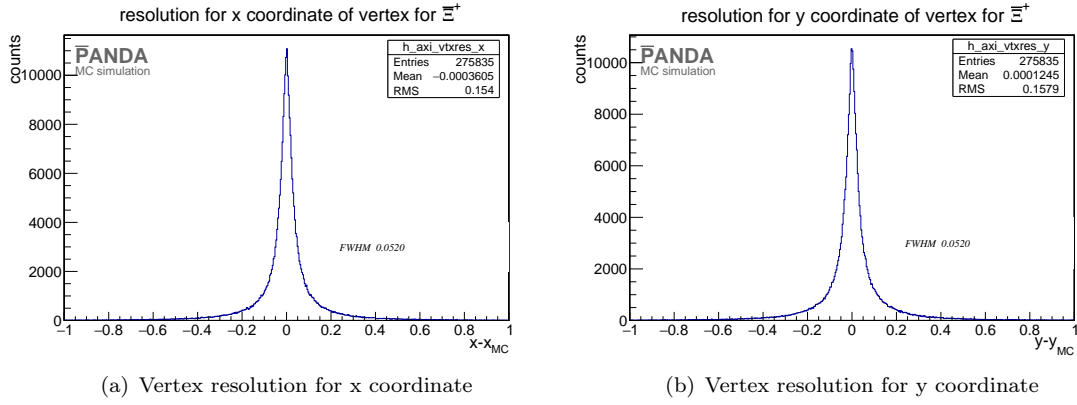


**Figure 3.11:** "PROPOSED FOR RELEASE" The left plot shows the vertex resolution in the x coordinate for  $\bar{\Xi}^+$ . The right plot shows the vertex resolution of in the y coordinate for  $\bar{\Xi}^+$ .

123 The advantage of using this method for calculating the vertex resolution is that the FWHM  
124 is independent of the shape of the distribution. Figures 3.11 and 3.12 show the vertex  
125 resolution distribution.

126 The mass distribution obtained with the different cuts is shown in figure 3.13 and figure  
127 3.14 for  $\bar{\Xi}^+$  and  $\Xi^-$ , respectively. The number of events is strongly reduced by the cut on  
128 the vertex fit probability. The width of the mass distribution is reduced.

129 After using all cuts on the mass distribution the reconstructed mass of  $\Xi^-$  and  $\bar{\Xi}^+$  can be  
130 determined by a double Gaussian fit. This is exemplarily shown for the  $\Xi^-$  in figure 3.15.

131 The result of the mass fit is for  $\bar{\Xi}^+$   $m = (1.322 \pm 0.004) \text{ GeV}/c^2$  and for  $\Xi^-$   
132  $m = (1.322 \pm 0.004) \text{ GeV}/c^2$ . The two dimensional momentum distribution for  $\bar{\Xi}^+$  and  $\Xi^-$   
133 is shown in figure 3.16

134 The reconstruction efficiency for  $\bar{\Xi}^+$  is 18.4% and for  $\Xi^-$  18.6%.

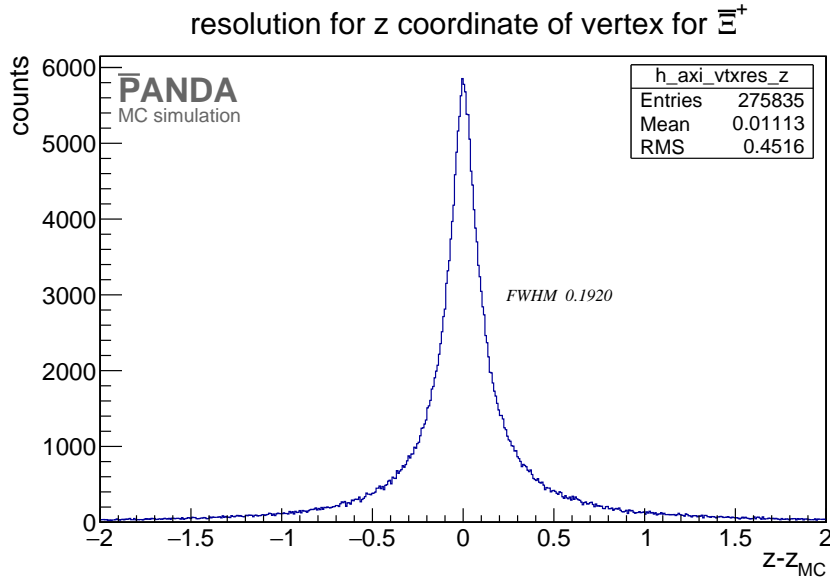


**Figure 3.12:** "PROPOSED FOR RELEASE" Vertex resolution of in the z coordinate for  $\Xi^+$  candidates.

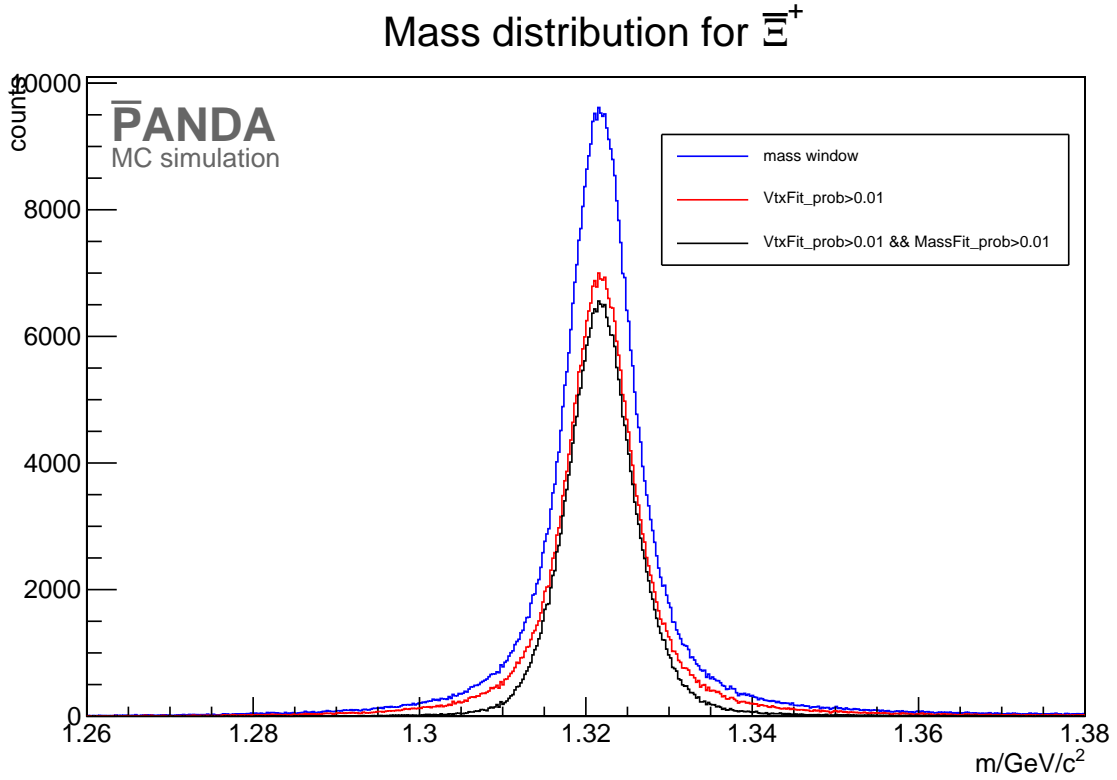


**Figure 3.13:** "PROPOSED FOR RELEASE" Mass distribution of the  $\Xi^+$  for different cuts: the mass cut is shown in blue, the vertex fit cut is shown in red and the distribution after all cuts is shown in black.

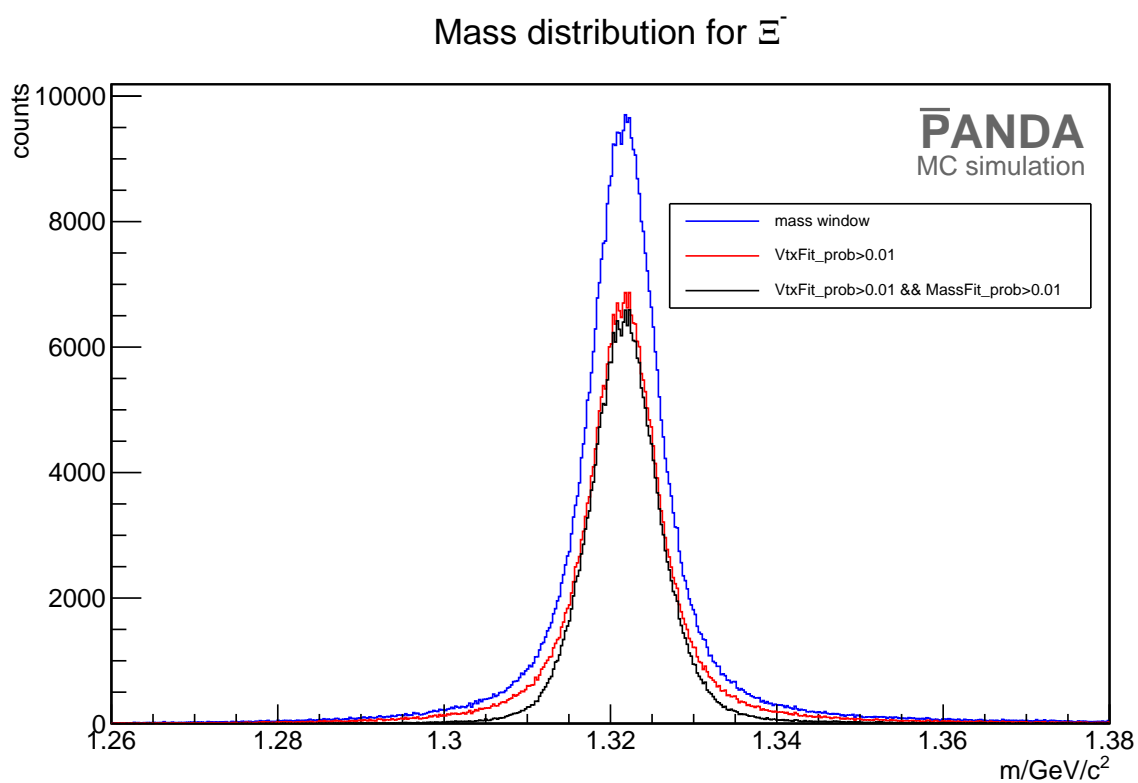


**Figure 3.14:** "PROPOSED FOR RELEASE" Mass distribution of the  $\Xi^-$  for different cuts: the mass cut is shown in blue, the vertex fit cut is shown in red and the distribution after all cuts is shown in black.

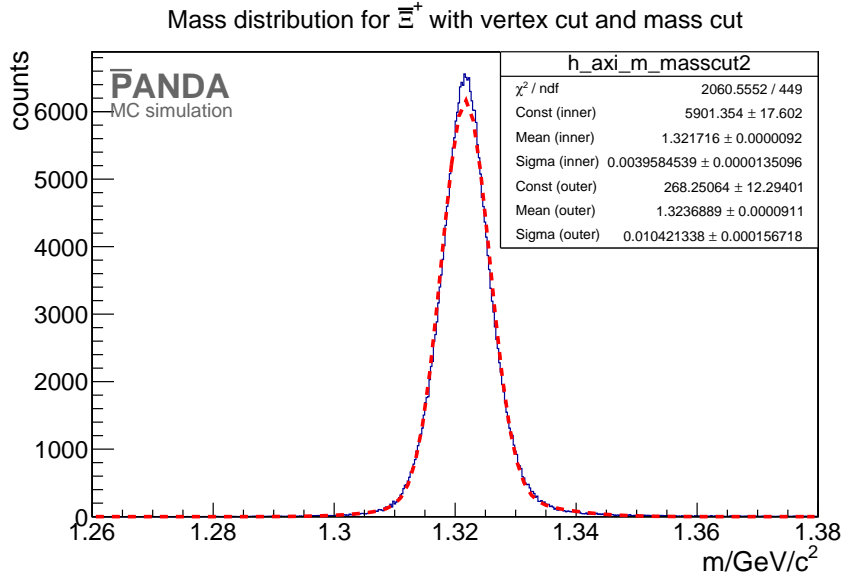


**Figure 3.15:** "PROPOSED FOR RELEASE" The plot shows the mass distribution (blue histogram) after all cuts. A double Gaussian fit (red dashed line) is performed to determine the mean reconstructed mass for the  $\Xi^+$ .

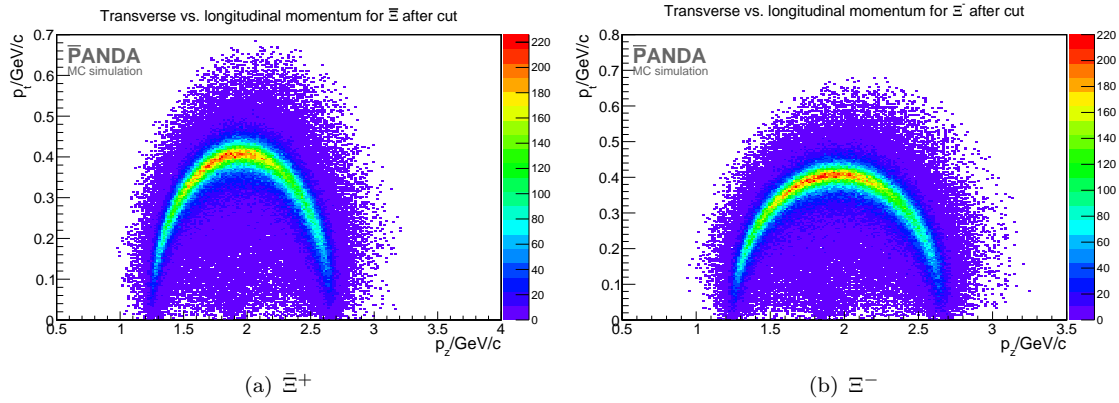


**Figure 3.16:** "PROPOSED FOR RELEASE" The plots shows the transverse versus the longitudinal momentum for  $\Xi^+$  and  $\Xi^-$

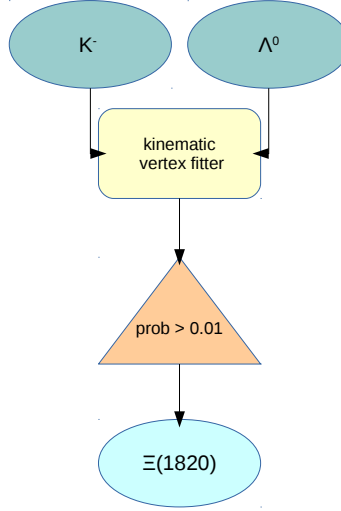


Figure 3.17: "PROPOSED FOR RELEASE" Scheme for  $\Xi(1820)^-$  reconstruction

### 3.4 Reconstruction of $\Xi(1820)^-$ and $\Xi^+(1820)$

#### Selection

For the reconstruction of  $\Xi(1820)^-$  one combines the  $\Lambda$  candidate with the  $K^-$  meson candidate and for  $\Xi^+(1820)$   $\bar{\Lambda}$  and  $K^+$ , using the fit candidates  $\Lambda$  and  $\bar{\Lambda}$ . After the combination of the particles a mass cut with a width of  $0.3 \text{ GeV}/c^2$  symmetric to the nominal  $\Xi(1820)^-$  mass is performed. The daughter particles are then fitted to a common vertex point with the PndKinVtxFitter. Only those candidates for  $\Xi(1820)^-$  ( $\Xi^+(1820)$ ) are selected which have a fit probability of more then 1%. The selection scheme is shown in figure 3.17.

The probability distribution for the vertex fit is shown in figure 3.18. Again the distribution is not flat but increases for values close to one.

If there is more than one particle the fit candidate with the smallest  $\chi^2$  is chosen.

#### Results

The vertex resolution for  $\Xi(1820)^-$  and  $\Xi^+(1820)$  is summarized in table 3.4.

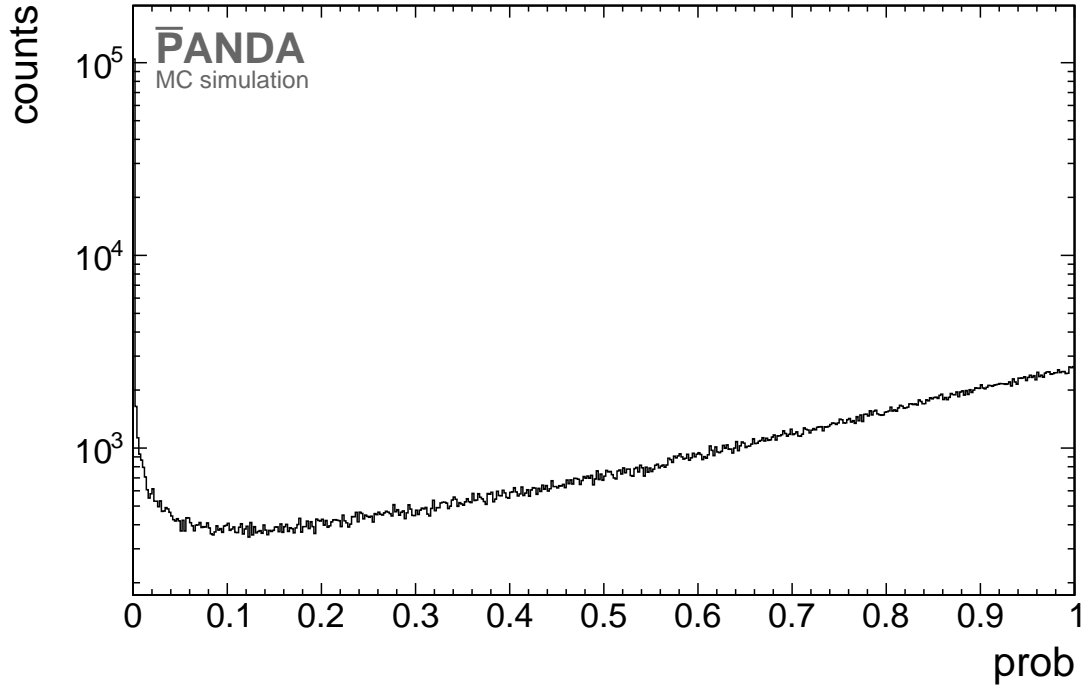
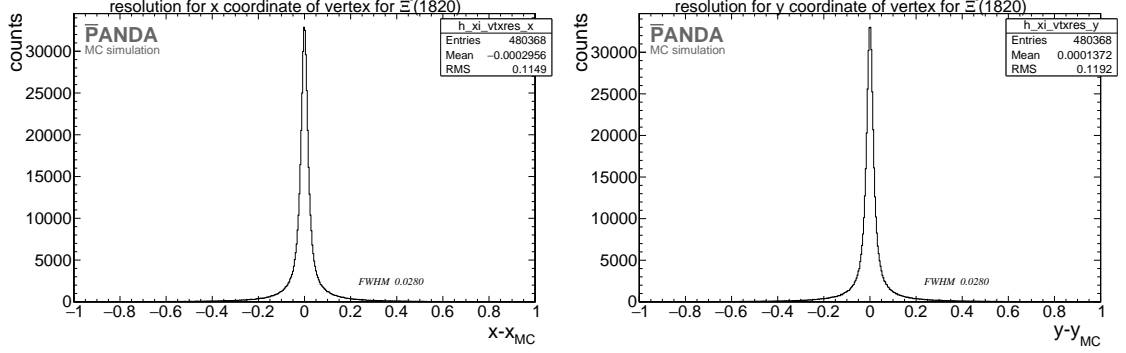


**Figure 3.18:** "PROPOSED FOR RELEASE" probability distribution of the kinematic vertex fit for  $\Xi(1820)^-$  candidates.

**Table 3.4:** "PROPOSED FOR RELEASE" Vertex resolution for  $\Xi(1820)^-$  and  $\Xi^+(1820)$ .

position	$\Xi(1820)^-$	$\Xi^+(1820)$ (from charge conjugate.)
x/cm	0.028	0.028
y/cm	0.028	0.028
z/cm	0.1	0.1

### 3.4. Reconstruction of $\Xi(1820)^-$ and $\bar{\Xi}^+(1820)$



(a) Vertex resolution of the x coordinate for  $\Xi(1820)^-$ . (b) Vertex resolution of the y coordinate for  $\Xi(1820)^-$ .

**Figure 3.19: "PROPOSED FOR RELEASE"** Figure a) shows the vertex resolution for the x coordinate and figure b) for the y coordinate of  $\Xi(1820)^-$

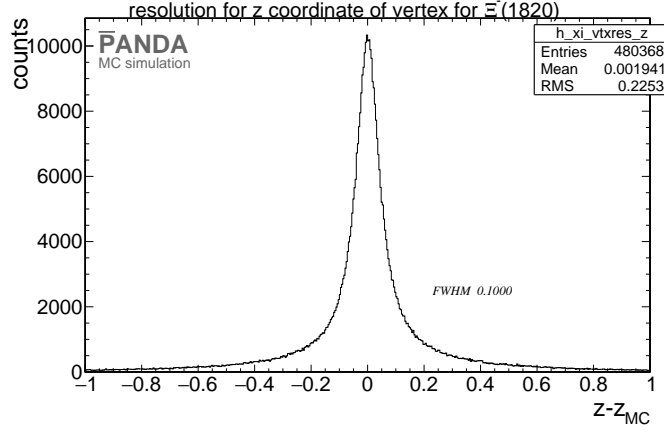


**Figure 3.20: "PROPOSED FOR RELEASE"** Vertex resolution in the z coordinate for  $\Xi(1820)^-$ .

149 Here again the vertex resolution is measured using the FWHM of the distribution. This is  
 150 exemplarily shown for  $\Xi(1820)^-$  in figure 3.19 and 3.20.

151 After performing both fits and cut on the probability values, the mass for  $\Xi(1820)^-$  and  
 152  $\bar{\Xi}^+(1820)$  can be determined by fitting with a double Gaussian function. Figure 3.21 shows  
 153 the mass distribution for both particles after each cut.

154 As an example the mass fit is shown for the  $\Xi(1820)^-$  in figure 3.22.

155 The mass value for the  $\Xi(1820)^-$  is fitted to  $m_{\Xi^*} = (1.8229 \pm 3.81 \cdot 10^{-5})$  GeV/c<sup>2</sup> and  
 156 for  $\bar{\Xi}^+(1820)$  to  $m_{\bar{\Xi}^*} = (1.823 \pm 3.73 \cdot 10^{-5})$  GeV/c<sup>2</sup>. These values are close to the input  
 157 value. Figure 3.23 shows the two-dimensional momentum distribution of  $p_t$  versus  $p_z$ .

158 The reconstructed distributions are in good agreement with the distribution obtained for  
 159 the generated events which are shown in figure 2.3 (b).

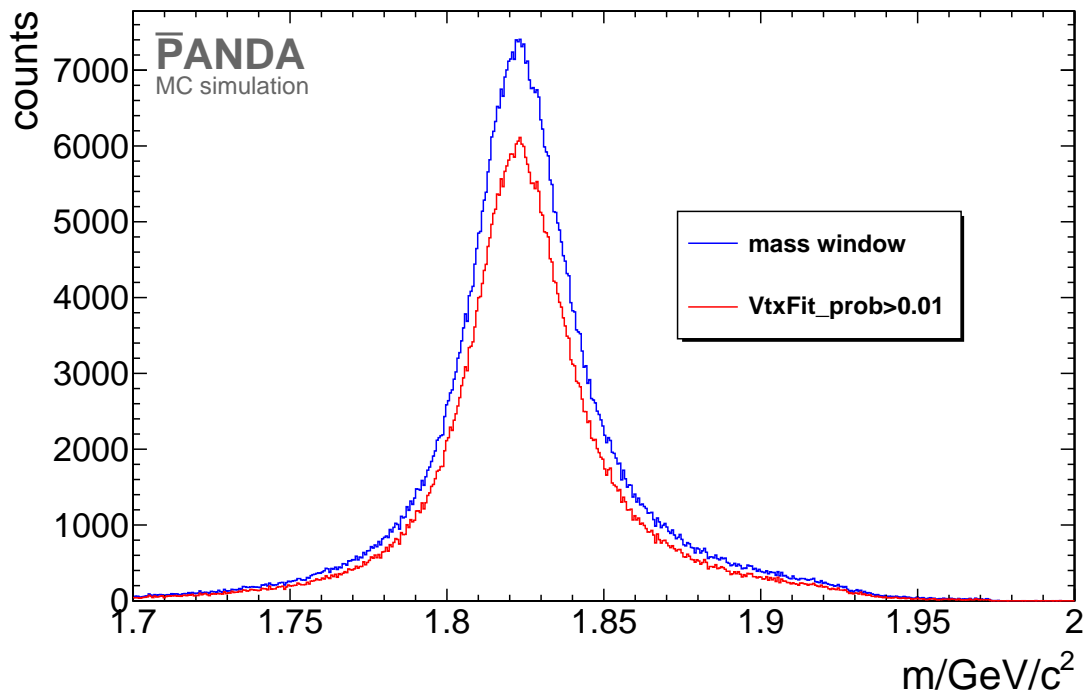


**Figure 3.21:** "PROPOSED FOR RELEASE" Mass distribution for  $\Xi(1820)^-$  after the mass cut in blue and after the vertex fit probability cut in red.



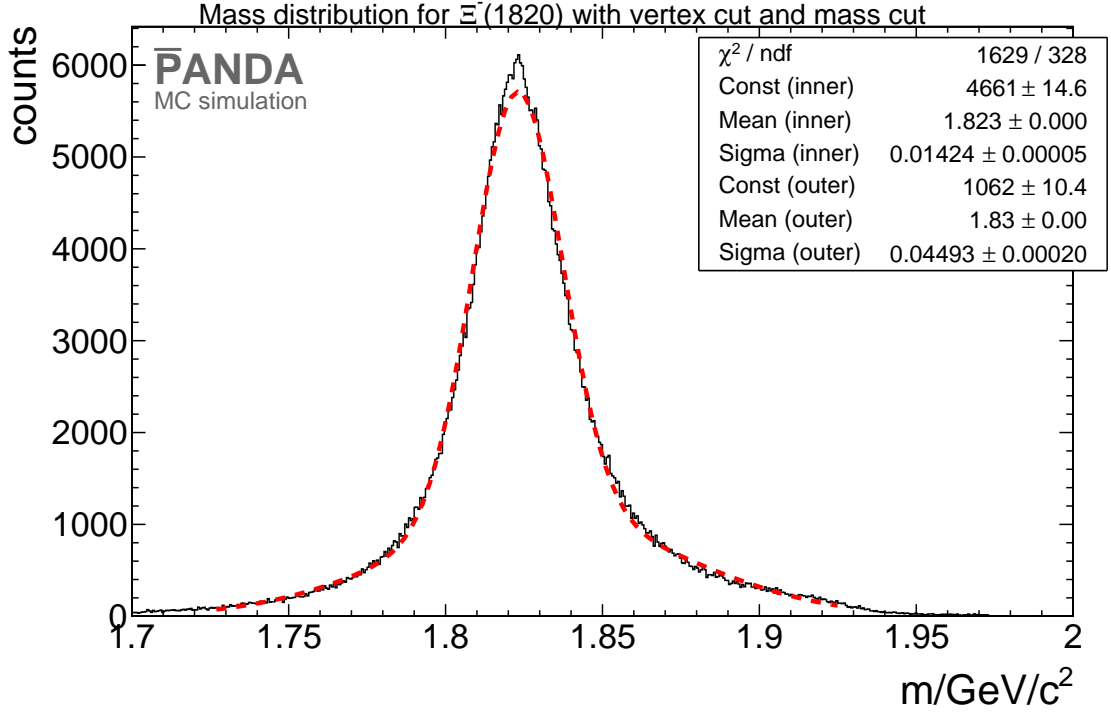


Figure 3.22: "PROPOSED FOR RELEASE" Mass distribution (blue histogram) after all cuts for  $\Xi(1820)^-$ . The performed double Gaussian fit is shown as the red dashed line.

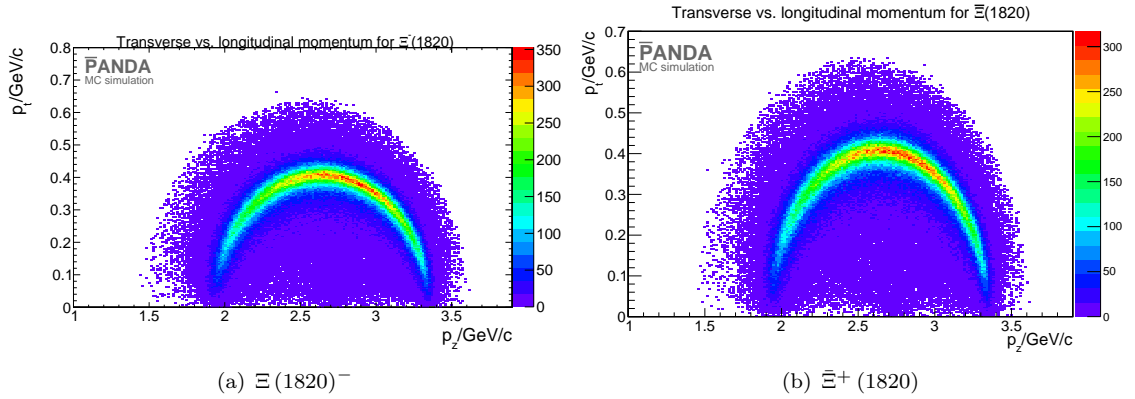
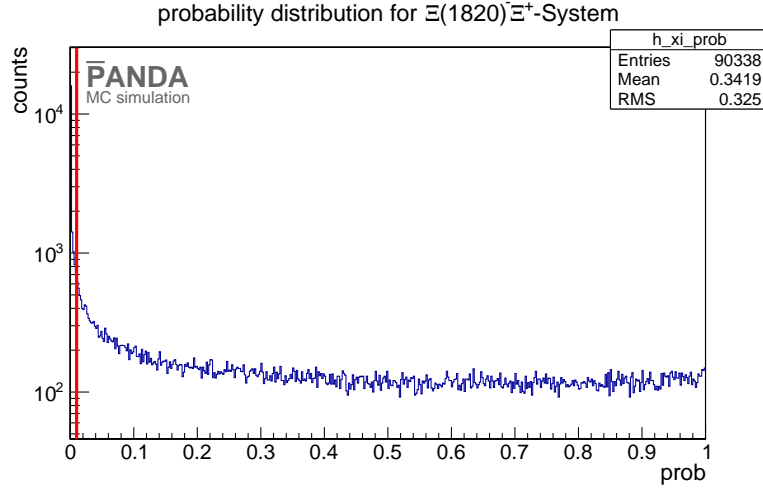


Figure 3.23: "PROPOSED FOR RELEASE" Both plots show the longitudinal versus the transverse momentum of the excited cascade baryon and its antiparticle, respectively.



**Figure 3.24:** "PROPOSED FOR RELEASE" 4-constraint fit probability. The red line denotes the cut value of 1%.

### 3.5 Reconstruction of the whole reaction chain

#### Selection

To reconstruct the whole reaction chain  $\Xi(1820)^-$  and  $\Xi^+$  are combined. This is also done with  $\Xi^+(1820)$  and  $\Xi^-$  for the charge conjugated channel. For this reconstruction the event selection is done with an exclusive method. The resulting four-momentum vector of both daughter particles – here  $\Xi(1820)^-$  and  $\Xi^+$  and there charge conjugate. particles – is fitted with the constraint to match to the initial four momentum vector

$$(p_x, p_y, p_z, E) = (0, 0, 4.6, 5.63) \text{ GeV}$$

of the  $\bar{p}p$  entrance channel. This fit is performed with the PndKinFitter. After the four-momentum fit only those candidates are selected which have a probability of more than 1%. The probability is shown in figure 3.24. The red line denotes the cut value.

The selection scheme is shown in figure 3.25

#### Results

The obtained reconstruction efficiency for all non-final state particles is shown in table 3.5 and table 3.6.

Figure 3.26 shows the Dalitz plot for the  $\Xi^+$ ,  $\Lambda$  and  $K^-$  final states after the reconstruction before the 4-C kinematic fit. Figure 3.26 should be compared with the Dalitz plot of the

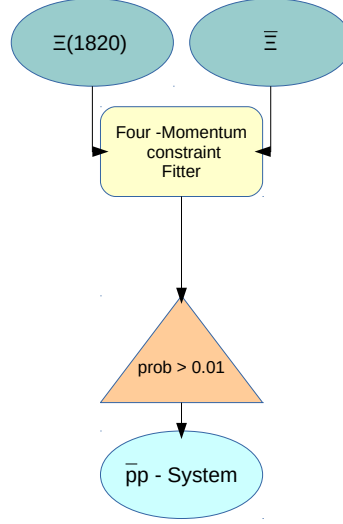


**Figure 3.25:** "PROPOSED FOR RELEASE" Scheme for the reconstruction of the whole reaction chain.

**Table 3.5:** "PROPOSED FOR RELEASE" reconstruction efficiency for non-final state particles for  $\bar{p}p \rightarrow \Xi(1820)^- \Xi^+$

particle	reco. efficiency in %	dp/p in %
$\Lambda$	40.5	1.40
$\bar{\Lambda}$	33.4	1.49
$\Xi^+$	18.4	1.29
$\Xi(1820)^-$	32.0	2.68
$\Xi(1820)^- \Xi^+$ system	4.7	1.03

**Table 3.6:** "PROPOSED FOR RELEASE" Reconstruction efficiency for non-final state particles for  $\bar{p}p \rightarrow \Xi^+(1820) \Xi^-$

particle	reco. efficiency in %	dp/p in %
$\Lambda$	32.8	1.44
$\bar{\Lambda}$	40.8	1.46
$\Xi^-$	18.6	2.30
$\Xi^+(1820)$	33.2	1.31
$\Xi^+(1820) \Xi^-$ system	4.9	1.03

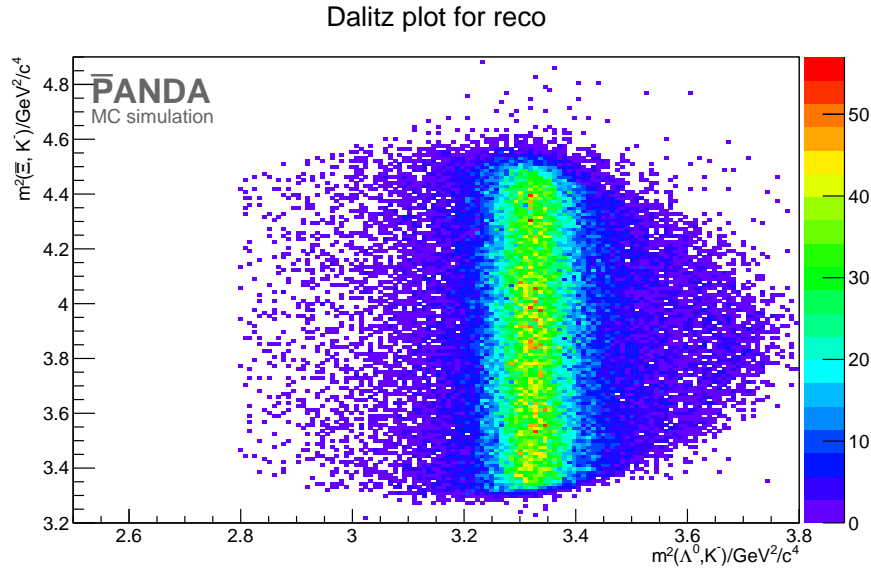


**Figure 3.26:** "PROPOSED FOR RELEASE" Dalitz plot for reconstructed  $\Xi^+ \Lambda K^-$  final state.

176 generated particles shown in figure 2.4 in order to assess the quality of the reconstruction  
 177 procedure.

---

## 178 4 Background

179 For background studies 15 million events have simulated with the Dual Parton Model based  
 180 generator DPM. To compare the number of selected events of background and signal, a  
 181 scaling factor is needed. This scaling factor can be calculated with the number of generated  
 182 events and the cross section of signal and background.

$$B = \frac{N_{\text{sig}}^{\text{gen}}/\sigma_{\text{sig}}}{N_{\text{bg}}^{\text{gen}}/\sigma_{\text{bg}}}, \quad (4.0.1)$$

183 where  $N_{\text{sig}}^{\text{gen}}$  is the number of generated signal events and  $N_{\text{bg}}^{\text{gen}}$  the number of generated  
 184 background events. The signal and background cross sections are given by  $\sigma_{\text{sig}} = 1 \mu\text{b}$   
 185 and  $\sigma_{\text{bg}} = 50 \text{ mb}$  [1], respectively. The scaling factor is  $B = 5000$  for the channel  $\bar{\text{p}}\text{p} \rightarrow$   
 186  $\Xi(1820)^- \bar{\Xi}^+$ . The scaling factor for the c.c. channel is the same. This means that the  
 187 number of reconstructed events in the background sample surviving all cuts applied to the  
 188 reconstruction of the signal events has to be multiplied by a factor 5000 in order to deduce  
 189 the achieved signal-to-background ratio.

190 All background events are subject to the same reconstruction procedure including all cuts  
 191 for the signal events. The number of reconstructed background events is shown in table  
 192 4.1.

193 The comparison between signal and background events is shown in table 4.2. The signifi-  
 194 cance is given by

$$S = \frac{N_{\text{sig}}^2}{N_{\text{sig}} + N_{\text{bg}} \cdot B}. \quad (4.0.2)$$

195 Because none of the background events survives the cuts applied to reconstruct the signal,

**Table 4.1:** Number of reconstructed background events for  $\bar{\text{p}}\text{p} \rightarrow \Xi(1820)^- \bar{\Xi}^+$

Particle	$N_{\text{bg}}$
$\Lambda$	264,142
$\bar{\Lambda}$	124,068
$\bar{\Xi}^+$	3,062
$\Xi(1820)^-$	298
$\Xi(1820)^- \bar{\Xi}^+$	0

**Table 4.2: "PROPOSED FOR RELEASE"** The number of background events scaled with factor  $B$  compared to the number of signal events for  $\bar{p}p \rightarrow \Xi(1820)^- \bar{\Xi}^+$ . The significance is calculated with equation 4.0.2.

Particle	$N_{\text{sig}}$	$N_{\text{bg}} \cdot B$	$S$
$\Lambda$	786,243	$1.321 \cdot 10^9$	467.68
$\bar{\Lambda}$	711,820	$620.341 \cdot 10^6$	815.85
$\bar{\Xi}^+$	302,681	$15.31 \cdot 10^6$	5,868.03
$\Xi(1820)^-$	490,672	$1.49 \cdot 10^6$	121,544.21
$\Xi(1820)^- \bar{\Xi}^+$	74,523	0	$> 69,837.37$

196 it is only possible to estimate a lower limit for the significance. For one background event  
197 scaled by the factor  $B$  the significance is at least 69,837.37. The signal-to-background ratio  
198 is for this estimation

$$\frac{N_{\text{sig}}}{N_{\text{bg}}} = \frac{74,523}{5000} = 14.9 : 1$$

199 To get a higher statistic more background events have to be generated.

---

## 5 Summary and Conclusion

The complete reaction chain can be reconstructed with an efficiency of about 5% for  $\bar{p}p \rightarrow \Xi(1820)^-$  and  $\bar{\Xi}^+$  and its charge conjugate channel.

Each final states particle has a reconstruction efficiency of nearly 80%. The reconstruction of  $\Lambda$  and  $\bar{\Lambda}$  shows a difference in the efficiencies. This is caused by the different mother particles of the  $\Lambda$  and  $\bar{\Lambda}$ . The reconstruction efficiency for  $\Lambda$  and  $\bar{\Lambda}$  might be improved by using the so-called lambda discs. However, this requires further studies which will be a part of future analysis.

The reconstructed mass for  $\Xi(1820)^-$  and  $\bar{\Xi}^+(1820)$  is in a good agreement with the literature value [3].

The topology of the decay chain suppresses the background efficiently. The comparison between the number of signal and background events shows how well background events can be suppressed by the selection criteria. After the reconstruction of the full reaction chain, the number of simulated signal events is 74,523 and the number of background events is zero. Assuming one single background event gives a limit for the significance of  $S > 69,837.37$ . For a more precise statement more background simulation is needed.

---

## References

- [1] W. Erni, I. Keshelashvili, B. Krusche, M. Steinacher, Y. Heng, Z. Liu, H. Liu, X. Shen, O. Wang, H. Xu, *et al.*, “Physics performance report for panda: Strong interaction studies with antiprotons,” *arXiv preprint arXiv:0903.3905*, 2009.
- [2] V. Flaminio, W. G. Moorhead, D. R. O. Morrisson, and N. Rivoire, “Cern report no. cern-hera84-01.” (unpublished), 1984.
- [3] K. A. Olive *et al.*, “Review of particle physics,” *Chin. Phys.*, vol. C38, p. 090001, 2014.
- [4] R. Kliemt. private communication, 2015.